UC Irvine
UC Irvine Previously Published Works

Title

Pathways Toward Efficient and Durable Anion Exchange Membrane Water Electrolyzers Enabled By Electro-Active Porous Transport Layers

Authors

Tricker, Andrew W

Ertugrul, Tugrul Y

Lee, Jason K

et al.

Peer reviewed

Pathways Toward Efficient and Durable Anion Exchange Membrane Water Electrolyzers Enabled By Electro-Active Porous Transport Layers

Andrew W. Tricker, Tugrul Y. Ertugrul, Jason K. Lee, Jason R. Shin, Woong Choi, Douglas I. Kushner, Guanzhi Wang, Jack Lang, Iryna V. Zenyuk, Adam Z. Weber, and Xiong Peng*

Green hydrogen, produced via water electrolysis using renewable electricity, will play a crucial role in decarbonizing industrial and heavy-duty transportation sectors. Anion exchange membrane water electrolyzers (AEMWEs) can overcome many of the performance and cost limitations of incumbent technologies, however, still suffer from durability challenges due to oxidative instability of anion-exchange ionomers. Herein, the use of an electro-active porous transport layer as anode (PTL-electrode) is demonstrated to enable efficient and durable AEMWEs. The stainless-steel PTL-electrodes are shown to have superior performance and durability compared to traditional catalyst layers containing ionomer and nanoparticle catalysts. An AEMWE cell operating at 2 A cm^{-2} for over 600 h exhibited a degradation rate of just 5 μV h^{-1}. During operation, the surface composition of the stainless steel transforms into a mixture of iron and nickel oxyhydroxides, contributing to enhanced oxygen-evolution reaction activity. The combination of experimental work and modeling elucidates how the bulk structure of the PTL-electrode offers an additional design dimension to further improve electrolyzer performance. Lastly, a surface modification strategy is applied to a PTL-electrode to achieve an even higher performing AEMWE (2.3 vs 2.0 A cm^{-2} at 1.8 V). Overall, this work lays out pathways toward more efficient, durable, and affordable AEMWEs.

1. Introduction

According to the Sixth Assessment Report of the Intergovernmental Panel on Climate Change, limiting the rise of global temperatures by 1.5 °C at the end of this century requires achieving global net-zero CO$_2$ emissions by 2050.[1] About one-third of global CO$_2$ emissions come from industrial processes (≈26%) and heavy-duty transportation (≈8%),[1–3] which are particularly difficult to decarbonize. Green hydrogen can play a unique role in achieving net zero for these sectors,[4] either as storage/carrier of renewable energy (e.g., fuel for freight transportation or industrial process heat),[5–8] as a replacement to fossil hydrogen (e.g., in petro/bio-refining or ammonia production),[9–13] or as an alternative chemical reagent (e.g., metal refining).[14] For this reason, the International Energy Agency has projected that the global usage of hydrogen will increase from 90 to 500 Mtpa (million tonnes per annum) to reach net zero by 2050.[15] Water electrolysis powered by renewable electricity is a promising approach to fill this demand, however, it supplies less than 1% of the current global market of hydrogen. With the global installed electrolyzer capacity estimated to be just 1 GW at the end of 2022,[16] achieving terawatt–scale deployment (1 TW ≈100 Mtpa H$_2$) will require electrolysis technology with high

A. W. Tricker, T. Y. Ertugrul, J. K. Lee, J. R. Shin, W. Choi, D. I. Kushner, G. Wang, A. Z. Weber, X. Peng
Energy Technology Area
Lawrence Berkeley National Laboratory
Berkeley, CA 94720, USA
E-mail: xiongp@lbl.gov

The ORCID identification number(s) for the author(s) of this article can be found under https://doi.org/10.1002/aenm.202303629

J. R. Shin
Department of Chemical & Biomolecular Engineering
University of California Berkeley
Berkeley, CA 94720, USA

J. Lang, I. V. Zenyuk
Department of Chemical and Biomolecular Engineering
National Fuel Cell Research Center
University of California Irvine
Irvine, CA 92697, USA

efficiency and durability, utilizing abundant and low-cost materials, and relying on components that are amenable to scalable manufacturability.

The incumbent commercial electrolyzers are liquid alkaline water electrolyzers (LAWEs) and proton-exchange membrane water electrolyzers (PEMWEs).[17] LAWEs rely on a concentrated aqueous hydroxide electrolyte (≈7 m) to conduct ions between the anode and cathode.[18] Thanks to the use of low-cost and durable cell components, LAWEs exhibit low capital expenditures and exceptional lifetimes. However, a porous separator is used to electronically separate the anode and cathode, and finite gaps between the electrodes and the separator are often necessary to minimize hydrogen crossover. This leads to large internal cell resistances and low operational efficiencies (0.1–0.3 A cm^{-2} at cell voltages of 1.8 –2.4 V),[18,19] which results in a high operating expense due to a high share of electricity costs to the levelized cost of produced hydrogen. In addition, the dynamic modes of operation by conventional LAWEs are often challenged by reverse currents as well as the safety restrictions from H$_2$ crossover at lower currents. PEMWEs utilize a proton exchange membrane to separate the anode oxygen evolution reactions (OER) and cathode hydrogen evolution reaction (HER) while conducting protons from the anode to the cathode in a zero-gap configuration,[20] which significantly reduces internal resistance and allows for much higher current (2–3 A cm^{-2}) operation at higher efficiencies compared to LAWEs, facilitating a wider range of applications and operating conditions. However, the acidic environment in PEMWEs necessitates the use of titanium for the bipolar plates and porous transport layers, which drives up capital costs,[21], and iridium-based OER catalysts, an expensive, low-abundance material that poses a potential bottleneck to wide-spread PEMWE deployment.[22]

Anion-exchange membrane water electrolyzers (AEMWEs) offer the benefits of low capital costs competitive to LAWEs and efficiencies competitive to PEMWEs,[23] though component durability remains a limitation. Under alkaline conditions, non-platinum group metal oxides can have comparable activities to iridium oxide for alkaline OER, and durable stack components can be made from nickel instead of titanium. The use of an AEM to achieve a zero-gap configuration significantly reduces internal cell resistances, compared to LAWEs, and allows for operation at higher current densities (>1 A cm^{-2}) while maintaining cell efficiencies above 82% (i.e., cell voltage ≤1.8 V), based on the higher heating value of hydrogen.[24,25] Although significant advances have been achieved in developing conductive and durable AEMs,[26] the electrode degradation still results in severe cell performance losses. Moreno–González et al. recently demonstrated a one-year operation of an AEMWE, with a degradation rate of 20 μV h^{-1} at 0.2 A cm^{-2} using nickel foam as the anode and cathode to isolate degradation from the membrane.[27] In the same study, an AEMWE using IrO$_x$ as an OER catalyst and Pt/C as an HER catalyst achieved an initial performance of 1.6 A cm^{-2} at 1.8 V, however, exhibited a degradation rate of nearly 1000 μV h^{-1} at 1 A cm^{-2} operation for 150 h. While others have demonstrated lower degradation rates for AEMWEs, these durability tests are generally conducted at relatively low current densities (≤1 A cm^{-2}) with typical rates still exceed 100 μV h^{-1}, which[24,28] are an order of magnitude greater than PEMWE degradation rates at ≈2 A cm^{-2}.[29] Therefore, developing robust electrodes as well as understanding the degradation

mechanisms remain as a grand challenge for the large-scale deployment of commercial AEMWE stacks for green hydrogen production.

Traditionally, to utilize more active catalysts and minimize ionic resistance, AEMWEs are often equipped with catalyst layers, where the catalyst nanoparticles are mixed with an anion exchange ionomer (AEI) that serves two main functions: to transport hydroxide ions (OH$^-$), and to bind the catalyst particles to form an intact catalyst layer. Various functional headgroup and backbone chemistries have been proposed to increase the OH$^-$ conductivity and AEI stability during electrolyzer operation.[30] For instance, imidazolium,[31,32] piperidinium,[33,34] and alkyl ammonium[35,36] cationic groups placed on ether-free polymer backbones have shown enhanced durability in AEM devices. However, the high alkalinity and oxidative condition at the anode still pose a potential challenge to the chemical and mechanical stability of AEIs, which can impact electrolyzer performance. As AEMWEs fed with supporting electrolytes achieve premium performance and durability, the ion-conducting feature of AEIs may have a negligible impact on device performance. Substantial efforts have been placed into developing methods to deposit novel catalysts[37] directly into the porous transport layers (PTLs) or identifying active materials, such as stainless steel,[38,39] for direct use as PTLs to avoid the presence of AEIs on the anode, primarily with a focus on studying the electrocatalytic performances. Recent work by Holdcroft and co-workers demonstrates the catalyst-layer free anode concept utilizing a stainless steel PTL as the OER catalyst achieves reasonable performance for AEMWEs.[40] This approach holds promise toward further reducing AEMWE costs, as it greatly simplifies the stack manufacturing process. However, less is known about the durability, scalability, structural impact, and performance relative to conventional catalyst layers.

In this work, the use of electro-active PTLs as an electrode (PTL-electrode) for achieving highly efficient and durable AEMWEs is demonstrated using commercially available materials. Comparisons of performance and stability between traditional catalyst layers and a stainless steel (S.S.) PTL-electrode is used to highlight the advantages of an electro-active PTL. In assessing industrial relevancy, scale-up (larger active area) and durability of the S.S. PTL-electrode are investigated. The role of the PTL-electrode structure has on the electrolyzer performance is elucidated through the combination of cell testing and continuum modeling. Finally, a facile modification approach is utilized to alter the surface of the electrode fibers to further highlight the prospects in achieving ever higher electrolyzer performance with an electro-active PTL-electrode.

2. Results and Discussion

2.1. PTL-Electrode Versus Traditional Catalyst Layer

First, three typical PTL-electrodes widely used in various water electrolyzer systems were studied: platinized titanium (Pt−Ti), nickel, and S.S. PTLs. The AEMWEs performance utilizing these PTL-electrodes for OER was studied in two supporting electrolyte conditions (Figure S1, Supporting Information). All three PTL-electrodes show electro-activity toward OER in alkaline media, with the S.S. demonstrating the highest activity, as evidenced by the lowest charge transfer resistance (Figure S2, Supporting
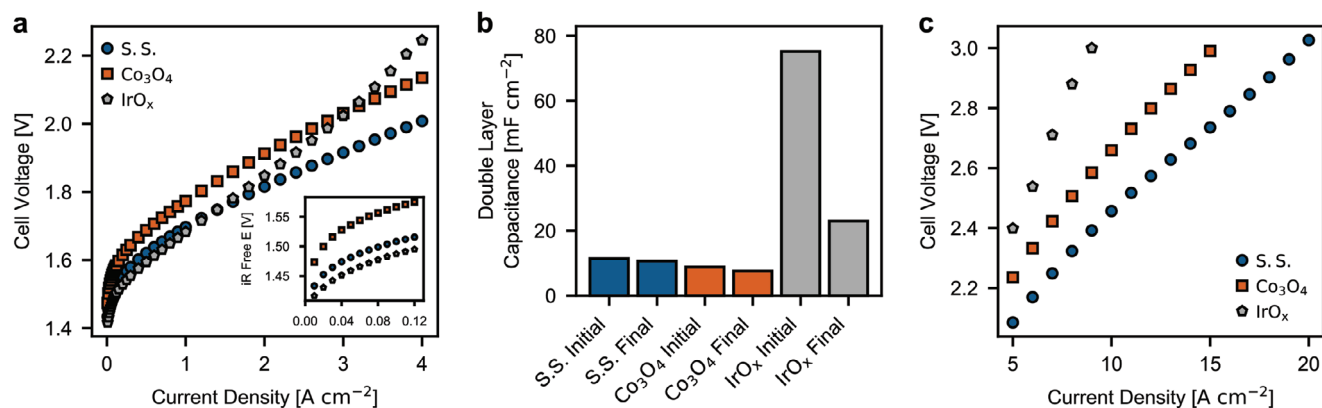
**ADVANCED
SCIENCE NEWS**

www.advancedsciencenews.com

**ADVANCED
ENERGY
MATERIALS**

www.advenergymat.de

Figure 1. a) Polarization curves of AEMWEs using a stainless-steel PTL-electrode (S.S.) and conventional catalyst layers of Co_3O_4 (2.0 mg cm^{-2}) and IrO_x (1.0 mg cm^{-2}) as anodes up to 4 A cm^{-2} Inlay shows the iR-free kinetic region. b) Double layer capacitances for each electrode measured at 80 °C in 1 M KOH. c) Polarization curves measured up to 3 V. Cathode: Pt/C (0.5 mg_{Pt} cm^{-2}), 1.0 M KOH; Anode: 1.0 M KOH; Membrane: 80 μm PiperION; 5 cm^2 active area; 80 °C.

Information) and device performance. The Pt—Ti PTL-electrode also exhibits measurable catalytic activity as a standalone electrode, but significantly less than S.S. (Figure S1, Supporting Information). The significant performance difference (0.44 V at 4 A cm^{-2}) between Pt—Ti PTL-electrode and catalysts coated Pt—Ti PTL confirms the AEMWE performance of the latter is mostly contributed by the coated catalyst layer (Figure S3a, Supporting Information), whereas the same case of S.S. PTL is negligible (Figure S3b, Supporting Information). These results suggest that in order to fairly evaluate the intrinsic OER activity of a catalyst in AEMWEs, PTLs with low electro-activity (such as a Ti-PTL) are suggested rather than more active S.S. PTLs.

Due to its exceptional performance, the S.S. PTL-electrode is chosen as the benchmark material in comparison with the traditional catalyst layers for AEMWEs. Additionally, since these S.S. PTL-electrodes can be used without further treatments, highly reproducible cell results can be achieved (Figure S4, Supporting Information), of course, when ensuring consistency of the cathode and AEM too. As the alkaline and oxidative conditions were expected to alter the elemental composition of the S.S., X-ray photoelectron spectroscopy (XPS) was used to probe the PTL-electrode surface (Figure S5, Supporting Information). It was found the surface was dominant with iron and nickel at an atomic ratio of 1:1, while the surface chromium was completely removed during testing. The iron was a mixture of FeO and Fe_2O_3 (1:3) and the nickel was a mixture of NiO(OH) and Ni_2O_3 (2:3). **Figure 1**a summarizes the performance comparison for AEMWEs using conventional catalyst layers of cobalt oxide (Co_3O_4) and iridium oxide (IrO_x) coated onto Pt—Ti PTLs versus the S.S. PTL-electrode. While Co_3O_4 is one of the more promising non-PGM catalysts for alkaline OER,[41] the S.S. outperforms the Co_3O_4 catalyst layer by 127 mV at 4 A cm^{-2}. Interestingly, the IrO_x shows the best kinetics (Figure 1a – inlay) and performance up to 1 A cm^{-2}, however the cell voltage drastically increases at higher current densities. Unlike the S.S. and Co_3O_4, degradation of the IrO_x catalyst layer did occur during the break-in procedure (Figure S6, Supporting Information), which was due to the loss of catalyst evidenced by the significant decrease in the double-layer capacitance (Figure 1b). Undoubtedly, the IrO_x exhibits greater intrinsic OER

catalytic activity compared to the S.S., however, since the reaction is concentrated in a thin catalyst layer ($\approx$25 μm), the large amount of gas and heat generated at higher current densities could lead to local pressure built-up and instability of the catalyst layer. The S.S. PTL-electrode, on the other hand, spreads the active surface area over a wider region (300 μm) such that surface gas blockage or local overheating becomes less detrimental.

To further verify this possibility, these three AEMWEs were polarized up to 3 V (Figure 1c). Here, the AEMWE using the S.S. PTL-electrode achieved a current density of 20 A cm^{-2}, one of the highest reported operational current densities for an AEMWE,[37] while exhibiting no tendency toward mass transport limitations. During measurement, the cell voltage remained steady during the 1 min operation at each current (Figure S7, Supporting Information). The AEMWEs with the IrO_x and Co_3O_4 catalyst layers achieved lower currents of 9 and 15 A cm^{-2} respectively. These results demonstrate the potential of using PTL-electrodes to achieve extremely high operational current density compared to conventional catalyst layers, potentially owing to the low volumetric density of reaction sites that are less sensitive to gas bubble blockage.

To further demonstrate the superiority of PTL-electrodes, the in-cell durability of PTL-electrodes and conventional catalyst layers in AEMWEs are compared utilizing accelerated stress tests (ASTs), a commonly used method to evaluate the durability of electrodes in electrolyzers.[42–44] The rapid cycling between operating conditions generally triggers more degradation of the catalyst layers, allowing for shorter experimental times and less conflation with the degradation of other components. Here, AEMWEs were subjected to square–wave current cycling of 5 s holds between 2 and 0.5 A cm^{-2} (**Figure 2**a) for a total of 30 k cycles, with polarization curves measured every 10 k cycles. First, the S.S. PTL-electrode was evaluated with the AST protocol (Figure 2b) with a dry cathode and 1.0 M KOH fed to the anode. The electrode exhibited excellent stability under AST, with the initial polarization curve (0 cycles) and ones measured every 10 k cycles overlaying very closely. At 2 A cm^{-2}, the cell voltage increased by just 14 mV, which occurred between the 10 and 30K cycles. XPS of the electrode after cycling shows minimal change
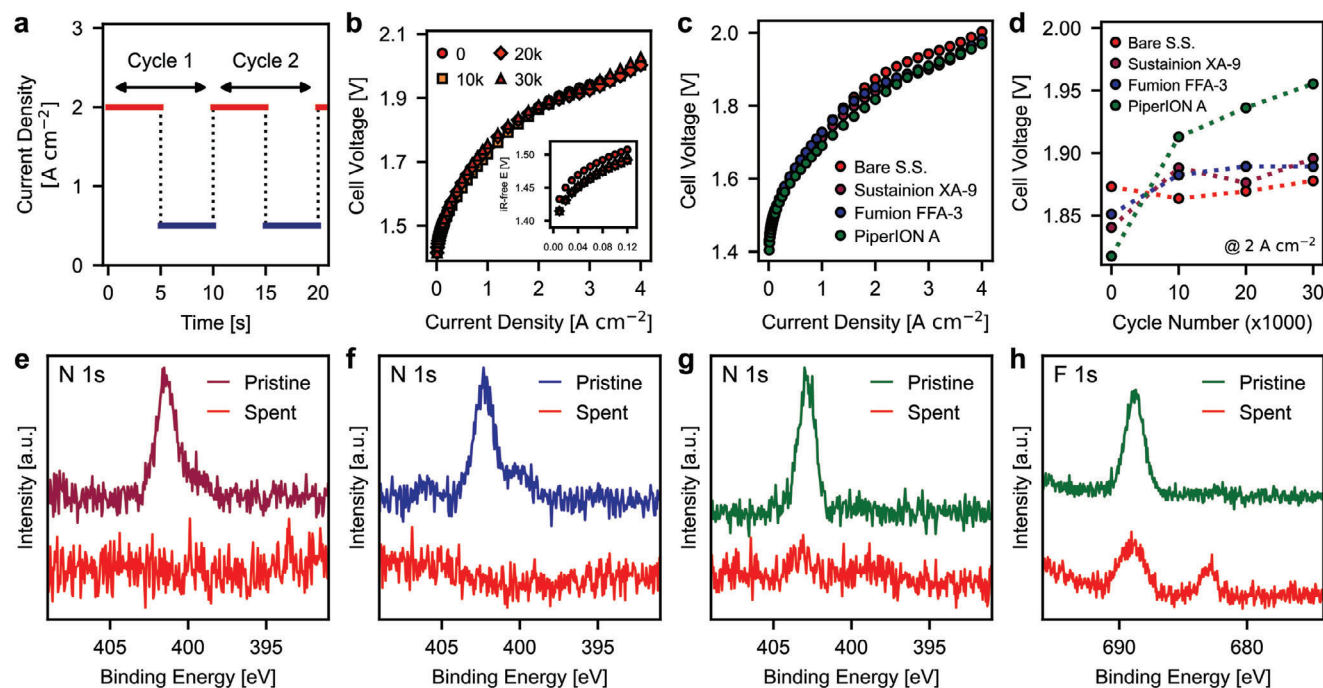
ADVANCED
SCIENCE NEWS

www.advancedsciencenews.com

ADVANCED
ENERGY
MATERIALS

www.advenergymat.de

Figure 2. a) AST protocol employing load cycling between 2 and 0.5 A cm^{-2}. b) Polarization curves using S.S. PTL-electrode as an anode during 30 k of ASTs. Inlay shows iR-free kinetic region. c) Initial polarizaiton curves using a PTL-electrode (Bare S.S.) or a S.S. PTL coated with Co$_3$O$_4$ catalyst layers with various ionomers as an anode. Cathode: Pt/C (0.65 mg$_{Pt}$ cm^{-2}), Dry; Anode: 1.0 M KOH; Membrane: 80 μm PiperION; 5 cm^2 active area; 80 °C. d) Cell volatage at 2 A cm^{-2} as measured during the polarization curve after every 10 k AST cycles. XPS spectra of the N 1s peak for the pristine and spent Co$_3$O$_4$ catalyst layers using, e) Sustainion, f) Fumion, and g) PiperION A as ionomers. h) XPS spectra of the F 1s peak for the pristine and spent Co$_3$O$_4$ catalyst layer using PiperION A as the ionomer.

in the nickel composition, while all the surface iron became Fe^{3+}, along with the formation of FeO(OH) (Figure S8, Supporting Information). The formation of FeO(OH) combined with NiO(OH) structure leads to a more active and stable OER catalyst phase,[45] which also corresponds to the improvement in the kinetic regime (Figure 2b – inlay) after the first 10 k cycles.

The same AST protocol was applied to S.S. PTLs coated with Co$_3$O$_4$ catalyst layers fabricated using three commercially available AEIs: Sustainion XA-9 (Dioxide Materials), Fumion FAA-3 (Fumatech), and PiperION A (Versogen). The chemistries of the three AEIs vary slightly: Sustainion and Fumion have imidazolium[46] and quaternary ammonium[47] sidechains, respectively, while PiperION has a piperidinium group integrated into the backbone.[33] PiperION and Sustainion both have hydrocarbon backbones, while Fumion has a poly(phenylene oxide) backbone. The initial polarization curves comparison (Figure 2c) shows that adding extra catalyst layer can achieve a 20 – 50 mV voltage reduction compared to S.S. PTL-electrodes at 2 A cm^{-2} among the three AEIs used. However, after the first 10 k cycles, this performance enhancement is lost (Figure 2d). The polarization curves for the Sustainion and Fumion electrodes stabilize after 10 k cycles at approximately the same cell voltage as the S.S. PTL-electrodes. The PiperION catalyst layer exhibited the best initial performance, however the cell performance continued to degrade with continued cycling. The full set of polarization curves is reported in the supplemental information (Figure S9, Supporting Information). XPS analysis of the catalyst layers after cycling shows extensive degradation of the ionomers: the ni-

trogen from the cationic functional headgroup is completely lost for each AEI (Figure 2e –g), along with changes of the fluorine group in PiperION A (Figure 2 h). Degradation of the Sustainion and Fumion AEIs in catalyst layers essentially results in a cell that solely relies on the activity of the S.S. PTL-electrode, with no synergistic benefit from the added catalyst layer. The continued loss of cell performance when using PiperION A, which potentially occurs from a poisoning effect from the degraded ionomer, also indicates that addition of these materials can result in adverse effects on durability. While AEI degradation can be anode catalyst dependent, Co$_3$O$_4$ has been shown to have the least detrimental effect.[41] Therefore, these results suggest that the lack of stability of AEIs under oxidative anode conditions still poses challenges for reliable AEMWEs even fed with support electrolytes, while the PTL-electrodes can achieve excellent performance and durability metrics with potential benefit in simplified MEA architecture and stack manufacturing process.

2.2. Industrial Applicability: Scale-Up and Durability

From an industrial perspective, developing reliable and high-throughput electrode manufacturing methods, such as roll-to-roll coating, is one of the most significant bottlenecks for deploying water electrolyzers at scale.[48,49] These challenges can be further exacerbated for AEMWEs if utilizing a conventional catalyst layer due to the lack of durable AEMs and AEIs
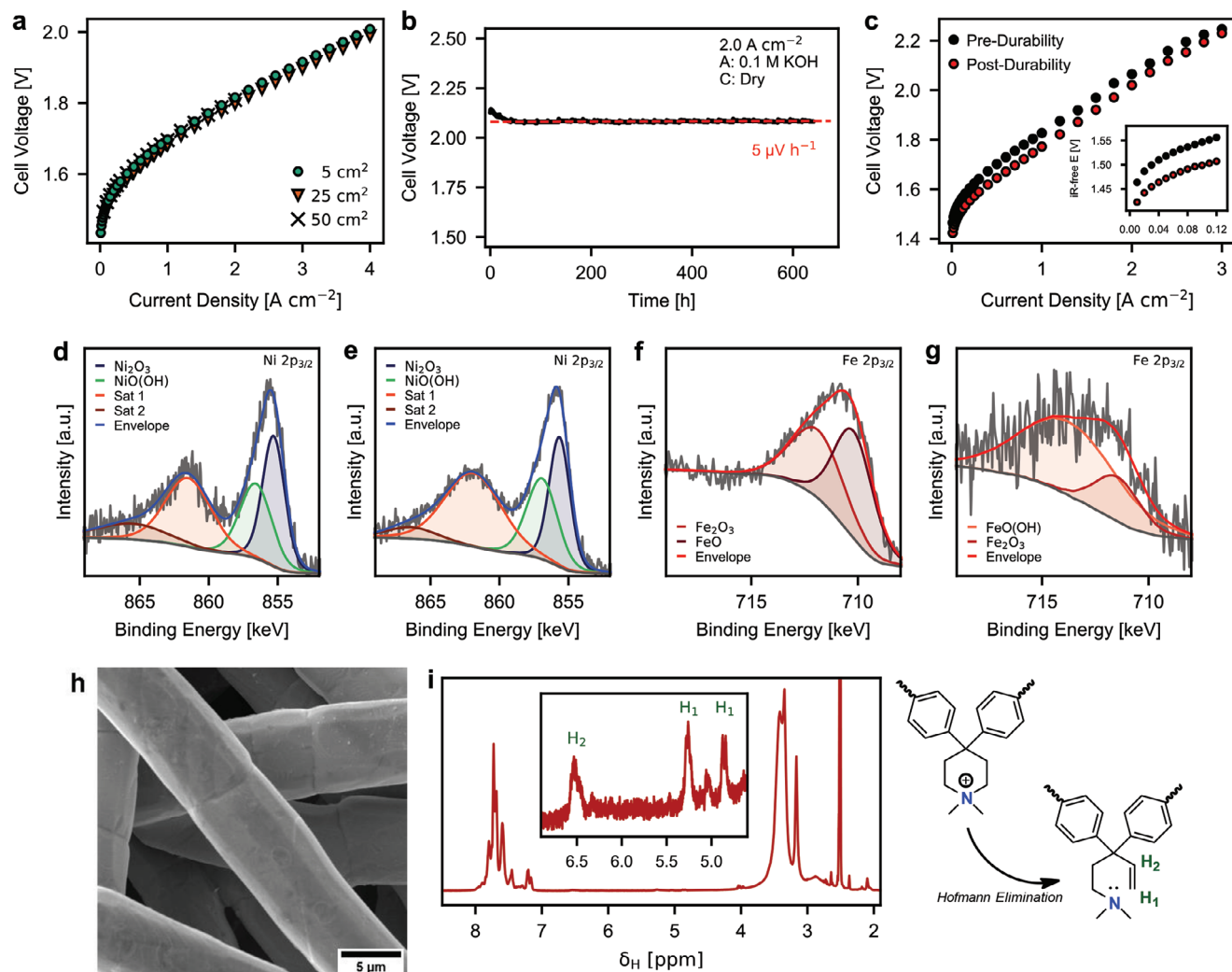
Figure 3. a) Polarization curves for 5, 25, and 50 cm² AEMWEs using S.S. PTL-electrodes as anodes. Cathode: Pt/C (0.5 mg$_{Pt}$ cm^{-2}), Membrane: 80 μm PiperION at 80 °C and 1.0 м KOH. b) AEMWE durability using S.S. PTL-electrode at current density of 2 A cm^{-2}. Red dashed line shows linear fit of the cell voltage after initial break-in. c) AEMWE polarization curves utilizing the pre-durability and the post-durability S.S. PTL-electrode, inset shows kinetic region. Cathode: Pt/C (0.65 mg$_{Pt}$ cm^{-2}), Dry; Anode: 0.1 м KOH; Membrane: 80 μm PiperION; 5 cm² active area; 80 °C. XPS spectra for the Ni$_{2s}$ peak of the d) pre- and e) post-durability electrode. XPS spectra for the Fe$_{2s}$ peak of the f) pre- and g) post-durability electrode. h) SEM image of electrode fibers post-durability. i) ¹H NMR spectra of the PiperION membrane post-durability and a schematic of the Hofmann elimination reaction for PiperION.

during stack manufacturing. For instance, AEMs/AEIs thermal degradation can be a risk due to accelerated nucleophilic attack reactions at drying conditions during roll-to-roll fabrication. As such, the replacement of traditional catalyst layers with PTL-electrodes removes one of the more challenging steps and presents an appealing approach to simplify and reduce the cost for electrolyzer stack manufacturing. In this section, the feasibility of operating AEMWEs using PTL-electrodes at large electrode sizes and the longevity under constant load conditions is demonstrated.

When scaling-up to larger active areas, liquid, and gas distribution across the flow field and PTL-electrode can start to play an increasing role in influencing electrolyzer performance. Potential inhomogeneities may have even greater impacts when a liquid electrolyte is necessary for maintaining ionic pathways to the OER sites within the PTL-electrode. As such, small active area cells (≤5 cm²) may not necessarily exhibit the same performance as larger cells, especially at higher current densities. The polarization curves for AEMWEs with active areas of 25 and 50 cm² were measured under the same conditions as the 5 cm² cell (**Figure 3a**). The performance of the 50 cm² cell could only be measured up to 2 A cm^{-2} due to the equipment's maximum operating current of 100 A. The AEMWEs at three different sizes perform nearly identically, achieving ≈2 A cm^{-2} at 1.8 V, showing the feasibility of operating high-performing AEMWEs at large electrode sizes using PTL-electrodes. Additionally, the experimental results from a 5 cm² electrode (e.g., durability or electrode modifications) will reasonably describe the performance of larger cells. Of course, translating single cell performance to stack performance still remains to be demonstrated, which can be leveraged by stack management practice from PEMWE[50–52] and LAWE[53] technologies.

**ADVANCED
SCIENCE NEWS**

www.advancedsciencenews.com

**ADVANCED
ENERGY
MATERIALS**

www.advenergymat.de

The durability of the S.S. PTL-electrodes was further investigated by holding a 5 cm² AEMWE at 2 A cm⁻². The cell was operated under a dry cathode condition and with 0.1 M KOH fed to the anode. After an initial break-in period (≈40 h), the cell voltage stabilized ≈2.08 V (Figure 3b). Perturbations in the cell voltage signal arose from replenishing cold DI water daily to the electrolyte bath, which led to small temperature fluctuations. The hydrogen crossover was measured every 200 h, with no appreciable change during the experiment (Figure S10, Supporting Information), indicating no significant membrane thinning through the test. The H_2 concentration in the O_2 stream ranged between 0.25% and 0.29%, similar to the crossover rates in PEMWEs and LAWEs.[54] Importantly, during the 600 h constant current hold at 2 A cm⁻², the cell voltage increased at a rate of just 5 µV h⁻¹, reaching a comparable durability performance to PEMWEs operating under similar conditions.[29]

The post-durability performance of PTL-electrode was evaluated by utilizing the spent PTL-electrode as the anode in a fresh AEMWE assembly (i.e., pristine membrane and cathode). The reassembled cell exhibited even better performance compared to the pre-durability performance (Figure 3c). Significant improvements in the kinetic region with the post-durability electrode (Figure 3c – inlay) suggest that prolonged exposure to the high potential and oxidative conditions can further activate the PTL-electrode. The pre-durability (after a single polarization curve in 0.1 M KOH) and post-durability PTL-electrode surface compositions were analyzed using XPS. The Ni 2p peak for both samples (Figure 3d,e) has contributions from NiO(OH) ≈858 eV[55] and Ni_2O_3 at 855 eV[56] with a marginal change in the relative abundance: 0.8:1 and 0.9:1 for the pre- and post-durability PTL-electrodes, respectively. For the pre-durability sample, the Fe 2p peak exhibits contributions from both Fe_2O_3 at 712 eV and FeO at 710 eV (Figure 3f),[57] which turns into FeO(OH) (714 eV) after the durability run (Figure 3 g).[58] This explains the improvement in anode activity due to the more active phase of FeO(OH) for OER in alkaline media,[45] which is also observed from the PTL-electrode after ASTs. It should also be noted that the abundance of Fe relative to Ni on the surface decreased from 2.4:1 to 0.7:1, which suggests a leaching out of surface Fe. However, SEM images of the post-durability PTL-electrode (Figure S11, Supporting Information) show that the fiber surfaces (Figure 3 h) remain intact and exhibit no significant roughening compared to the pristine sample, indicating the Fe leaching could occur only during an initial break-in period (≈40 h), after which a stable and active OER phase forms.

While the cell exhibited low overall degradation, exploring changes of the cathode and AEM resulting from these operating conditions could elucidate additional information on degradation modes and pave the way for future design toward more durable AEMWEs. For the cathode, there is only a marginal loss of platinum (≈2%), as measured by X-ray fluorescence spectroscopy (Figure S12, Supporting Information), which is in the margin of error for the instrumentation. XPS shows a decrease in the nitrogen and fluorine content (Table S1, Supporting Information), relative to platinum, as well as changes to the N 1s peak (Figure S13, Supporting Information), indicating that degradation of the cathode AEI did occur. Additionally, chromium as well as trace amount of iron was detected on the cathode (Figure S14, Supporting Information), which was formed due to redeposition of

dissolved species from the anode. Proton nuclear magnetic resonance spectroscopy ([1] H NMR) of the post-durability membrane shows peaks corresponding to the H−C≡C (δ_H = 6.5 ppm) and C=C−H_2 (δ_H = 5.25 ppm, 4.85 ppm), resulting from Hofmann elimination of the piperidinium functional group (Figure 3i),[59] however with only a loss of 6% of the functional groups. The occurrence of the Hofmann elimination is further supported by Fourier-transform infrared spectroscopy (FTIR) with the peak shift from 1620 to 1605 cm⁻¹ between the fresh and spent membrane (Figure S15, Supporting Information), indicating the formation of new C=C bonds.[60] Possible degradation mechanism of the membrane can result from oxidation due to the direct contact between the membrane and the electrode and the presence of trace Fe ions in the electrolyte (i.e., Fenton reaction).[61] While reactions of the polymer backbone did occur, evidenced by the appearance of new peaks in the aromatic region of the 2D Heteronuclear single quantum coherence (HSQC) NMR spectrum (Figure S16, Supporting Information), the exact degradation mechanism would require further investigation.

2.3. Impacts of the Macrostructure of the Electro-Active PTL

The utilization of the whole PTL architecture as a catalytically active electrode offers an opportunity to fine-tune its critical structural parameters and provide additional design dimensions for engineering improved device performance, which can be challenging for conventional catalyst layers due to the complicated impacts by catalyst ink rheology and fabrication conditions. To illustrate this, two PTL-electrodes were selected: a single layer PTL-electrode with 8 µm diameter fibers (**Figure 4a**) and a bilayer PTL-electrode with a layer of 4 µm diameter fibers (4-d-L) and a layer of 8 µm diameter fibers (8-d-L) (Figure 4b). The structures of the PTLs were characterized in detail using X-ray computed tomography (XCT), with structural parameters reported in Table S2 (Supporting Information). For both PTL-electrodes, the porosity remains identical (75% – 78%) throughout the whole thickness (Figure 4c). The pore size distributions were also calculated for each layer (Figure 4d). The single layer PTL-electrode has average pore radii of 8.70 µm, whereas the bilayer PTL-electrode has average pore radii of 8.55 and 6.42 µm for the 8-d-L and 4-d-L, respectively. The through-plane tortuosity was calculated to be 1.03 for the single layer PTL and 1.19 and 1.04 for the 8-d-L and 4-d-L of the bilayer PTL-electrode, respectively.

The performance of AEMWEs using the single layer PTL-electrode (SL_8) was compared to two configurations of the bilayer PTL-electrodes: one with the 4-d-L facing the AEM (BL_8-4) and another with the 4-d-L facing the flow field (BL_4-8) (Figure 4e). The presence of the 4-d-L close to the AEM (BL_8-4) increases the performance compared to the single-layer electrode (SL_8) (Figure 4f). Since the performance improvement is mostly seen at high current region (10– 20 A cm⁻²), it suggests an improvement from mass transport mainly attributed to better gas bubble management resulting from the 4-d-L located closer to the membrane, which has also been previously reported for bilayer PTLs in PEMWEs[62,63] and AEMWEs with catalyst layers.[64,65] Gas, being a non-wetting phase, tends to invade pores with larger openings under capillary dominated flow regime, and therefore having a layer with smaller pore radii results in lower gas
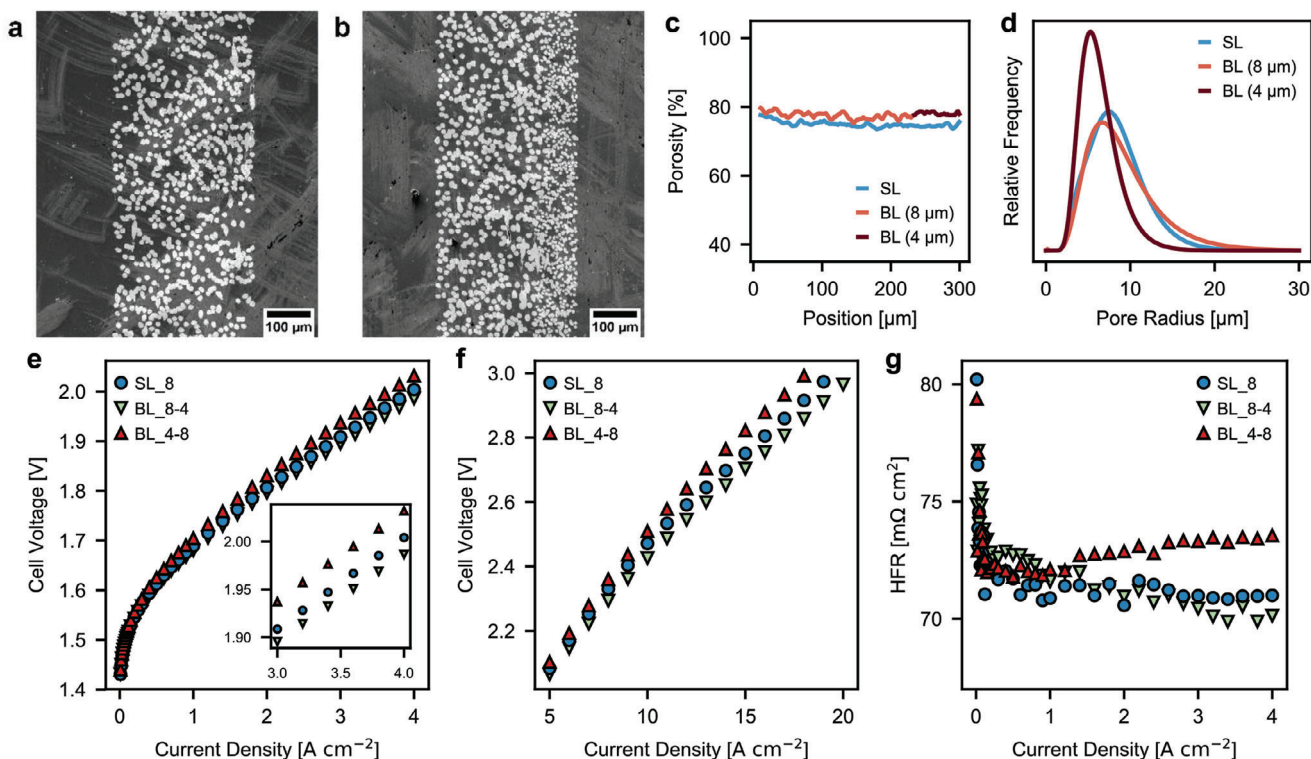
Figure 4. Cross-sectional SEM images for a) the 8 μm fiber single layer PTL-electrode and b) the 4/8 μm fiber bilayer PTL-electrode. c) Through-plane porosity of the single layer and bilayer PTL-electrodes. d) Pore size distributions of the single layer PTL-electrode (SL) and the 8 and 4 μm fiber layers of the bilayer PTL-electrode (BL). Polarization curve e) up to 4 A cm^{-2}; f) up to 20 A cm^{-2} and g) HFR for AEMWEs using the single layer PTL-electrode (SL_8), the 4/8 μm fiber bilayer PTL-electrode with the 4 μm diameter fibers facing the membrane (BL_8-4), and the 4/8 μm fiber bilayer PTL-electrode with the 8 μm diameter fibers facing the membrane (BL_4-8) as anodes. Anolyte/catholyte: 1 M KOH, cathode: Pt/C (0.5 mg$_{Pt}$ cm^{-2}); 80 μm PiperION membrane; 5 cm^2; 80 °C.

saturation and, in turn, fewer liquid electrolyte voids within the 4-d-L of the bilayer PTL-electrode. Since the aqueous electrolyte provides only reaction interfaces and ionic pathways, voids in the electrolyte resulting from the gas generation can lead to isolated regions without electrolyte supply as well as increase the ionic resistance within the electrode.[66]

In case where the 4-d-L is facing the flow field (BL_4-8), a decrease in cell performance is observed as gas removal can be restricted and trapped near the AEM. Placing the 8-d-L with larger pore radii next to the AEM encourages gases to invade pores adjacent to each other before advancing into the 4-d-L, therefore increasing the electrolyte void space, which leads to an increase in the ionic resistance at higher currents and a decrease in PTL-electrode utilization. This gas filling of the 8-d-L is further supported by the increase of HFR for BL_4-8 at higher current densities (Figure 4 g),[63] potentially due to impacting the supply of electrolyte to the AEM.

To gain additional insights into how the structure and configuration of the PTL-electrode affect cell performance, a 1D AEMWE model[67–68] was utilized to elucidate the effects for these three test configurations. The model incorporates conservation equations (mass, momentum, energy, charge, and species) along with Butler–Volver kinetics to calculate polarization curves and spatial distributions of various properties within the electrolyzer. Additionally, an empirical correlation was used to estimate local bubble generation in the PTL-electrode. Bubble coverage was

adapted to approximate the effective surface area and OH$^-$ conductivity values. The model results were first calibrated using the experimental polarization curves (Figure S17, Supporting Information), with key parameters employed in the model listed in Table S3 (Supporting Information). The three pieces of information that best describe the difference in cell performance are the reaction current (the amount of reaction occurring per unit volume), bubble coverage of the electrode surface, and the apparent ionic conductivity of the electrolyte, which are shown as a function of position within the electrode for each cell configuration at voltage of 1.9 V (**Figure 5**).

For these PTL-electrodes, the most utilized region is closest to the AEM (Figure 5a), with current contribution decreasing closer to the flow field due to increasing ionic resistance far from the AEM. However, despite the uneven distribution of currents across the PTL-electrode, the whole architecture still contributes significantly to the overall current density. Though the reaction current distribution shows that the increased performance of BL_8–4 is mostly contributed by the 4-d-L, the higher utilization 4-d-L does not lead to higher bubble coverage to the electrode surface due to higher surface area from smaller fiber diameters (Figure 5b). The lower bubble coverage also creates fewer void spaces and therefore increases the effective ionic conductivity of the electrolyte within the 4-d-L for BL_8-4 (Figure 5c), which ultimately contributes to the improved performance. For BL_4–8, the amount of reaction occurring right near the AEM is identical

**ADVANCED
SCIENCE NEWS**

www.advancedsciencenews.com
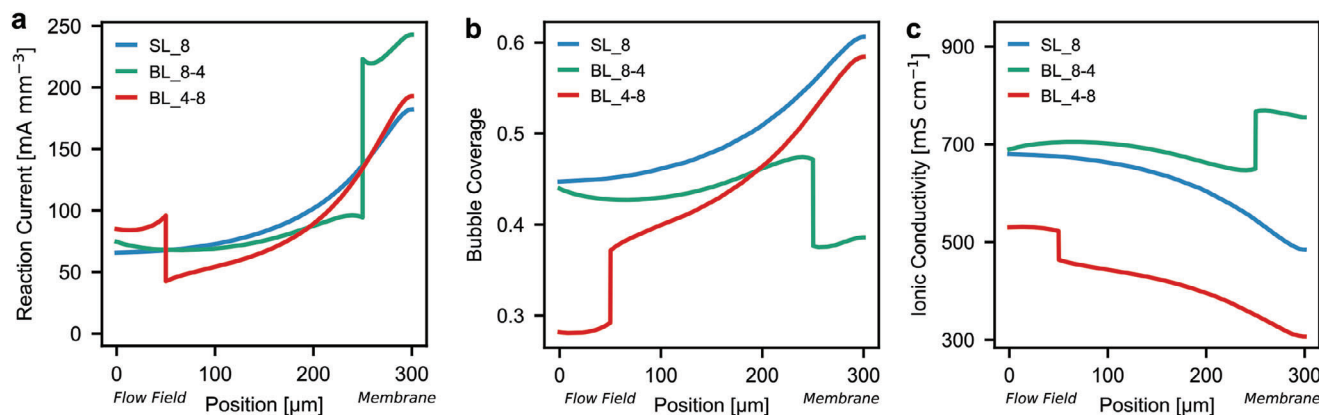
**ADVANCED
ENERGY
MATERIALS**

www.advenergymat.de

Figure 5. a) Reaction current, b) catalyst surface bubble coverage, and c) effective ionic conductivity throughout the electrode for the single layer PTL-electrode (SL_8), the bilayer PTL-electrodes with the 4 µm diameter fibers facing the membrane (BL_8-4), and the bilayer PTL with the 8 µm diameter fibers facing the flow field (BL_4-8) at a cell voltage of 1.9 V. The flow field is at position 0 µm and the membrane is at position 300 µm.

to that of SL_8, which is expected given the similarity in pore radii and fiber diameter of the single layer PTL-electrode and the 8-d-L of the bilayer PTL-electrode. While the productivity is similar adjacent to the AEM, the amount of reaction decreases to a greater extent for BL_4–8 owing to the lower ionic conductivity within the PTL-electrode, resulted from the above mentioned bubble trapping effect and a more tortuous through-plane ionic conducting pathway shown by XCT measurements (1.19 vs1.03). Overall, the combination of experimental and modeling results shows that the structural features of PTL-electrodes can impact electrode spatial utilization and effective ionic conductivity as a result of bubble dynamics and electrolyte supply, which are critical to AEMWEs performance.

2.4. Approach to Improving PTL-Electrode AEMWE Performance

Beyond its structural parameters, the surface characteristics of the PTL-electrode can be fine-tuned to further improve the AEMWE performance. As a demonstration, a pristine S.S. PTL-electrode was treated in a 60 °C bath of nitric acid (10 wt%) and hydrochloric acid (3 wt%) for 10 min – a process based on industrial pickling treatment.[69] Comparisons of the pristine fibers (**Figure 6a**) and the treated fibers (Figure 6b) show a significantly roughened surface, which increases the surface area for OER. The pickling process removed 20% of the sample mass, indicating these modified fiber surface features can be present throughout the whole electrode architecture. Additionally, the pickling did result in a compositional change to the fiber surfaces with a preference toward dissolving iron. Based on XPS, the Cr: Fe surface composition of the fibers increased from 0.12:1 before treatment up to 1.5:1 after pickling (Figure S18, Supporting Information). The presence of nickel was still not meaningfully measured by XPS even after acid treatment due to the limit in penetration depth of the measurements.

To directly evaluate the impact of pickling on the OER activity, linear sweep voltammetry (LSV) measurements were conducted using pristine and pickled PTL-electrodes samples in a three-electrode cell (1 м KOH, room temperature). The treated sample showed a clear increase in OER activity with a lower onset poten-

tial and a reduction in overpotential of 20 mV at 100 mA cm⁻² (Figure 6c). The improved kinetics of the treated PTL-electrode translated to improved AEMWE cell performance (Figure 5d), achieving 2.3 A cm⁻² at a cell voltage of 1.8 V (or 82% efficiency). Lower voltages in the kinetic region of the cell polarization curve (Figure 6d – inlay) and a decrease in the charge-transfer resistance from EIS (Figure 6e) also indicate improved electrode kinetics, which corresponds well to the three-electrode measurement. After cell testing, the chemical composition of the pristine and pickled PTL-electrodes was identical (Figure S19, Supporting Information), therefore the activity improvement is predominantly attributed to the change in the fiber surface area. The efficacy of the acid treatment of PTL-electrode to improve AEMWE performance was further demonstrated using bilayer PTL-electrode (BL_8-4), where similar cell performance improvements were observed (Figure S20, Supporting Information). A short-term durability test was conducted using the pickled PTL-electrode at 2 A cm⁻² with 0.1 м KOH fed to anode (Figure S21, Supporting Information). The treated PTL-electrode shows negligible degradation, which further indicates the promise of pickling in developing active and durable PTL-electrodes.

3. Conclusion

In summary, this work demonstrates highly efficient and durable anode catalyst-layer-free AEMWEs enabled by electro-active PTL-electrode. Comparison of the PTL-electrode to traditional catalyst layers, utilizing Co_3O_4 or IrO_x catalyst with AEIs, shows the PTL-electrode achieves better cell performance and durability under accelerated stress testing (AST). Traditional catalyst layers face durability challenges owing to the oxidative instability of AEIs under anode operating conditions. AEMWEs using the S.S. PTL-electrode show negligible performance difference between and 50 cm² size, which suggests its promising scale-up potential. The S.S. PTL-electrode achieved excellent stability at 2 A cm⁻² fed with dilute anolyte (0.1м KOH) for 640 h, with an average degradation rate of just 5 µV h⁻¹, ranking one of the best-reported AEMWEs durability. The AST and durability tests suggest a self-activation mechanism could occur during electrolysis operation, resulting from the formation of FeO(OH) and NiO(OH) phases,
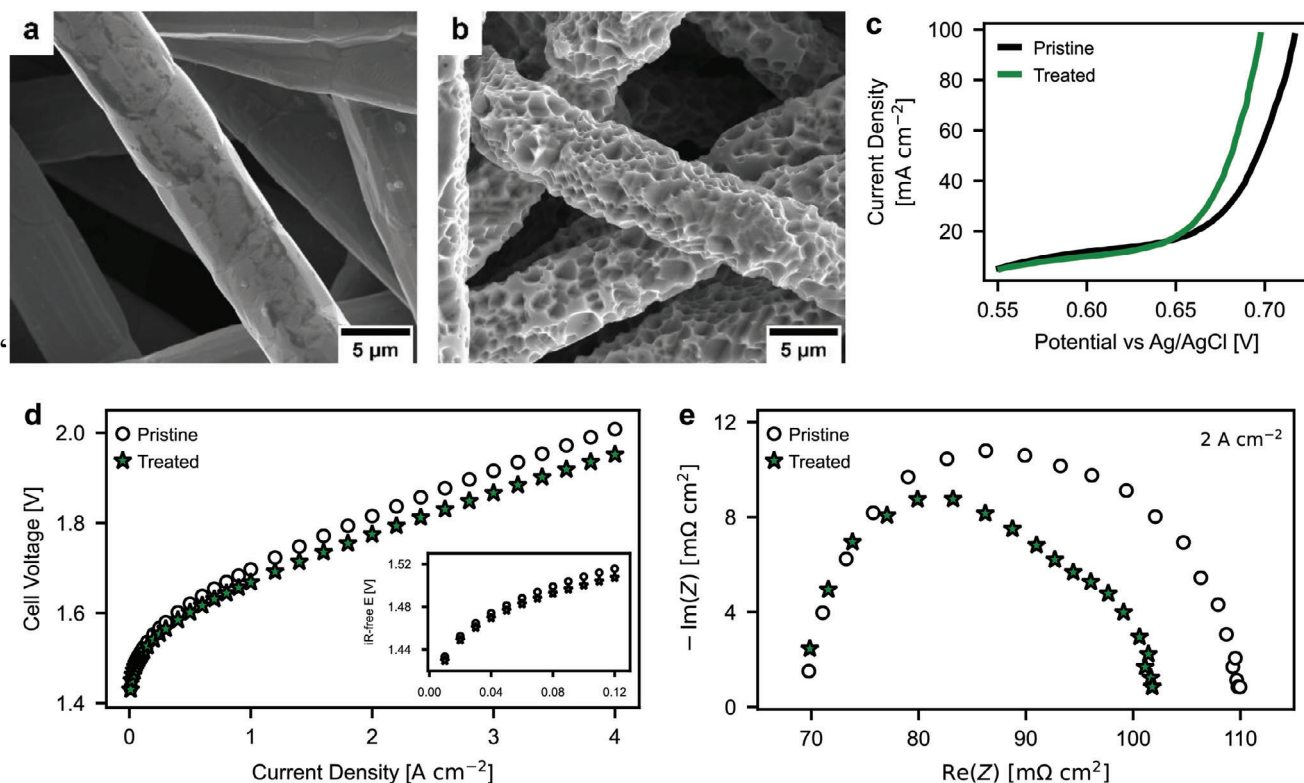
**ADVANCED
SCIENCE NEWS**

www.advancedsciencenews.com

**ADVANCED
ENERGY
MATERIALS**

www.advenergymat.de

Figure 6. SEM images of the a) initial stainless-steel PTL-electrode fibers (Pristine) and b) pickled stainless steel PTL-eectrode fibers (Treated). c) *iR*-corrected linear sweep voltammetry measurements of the pristine and acid-treated PTL-electrodes in 1 M KOH at room temperature. d) Polarization curves and e) EIS spectra at 2 A cm^{-2} for AEMWEs using the pristine and treated stainless steel PTL-electrodes. Anolyte/catholyte: 1 M KOH, cathode: Pt/C (0.5 mg$_{Pt}$ cm^{-2}); 80 µm PiperION A membrane; 5 cm^2; 80 °C. Inlay shows the *iR*-free kinetic region.

which are more active for OER, on the PTL-electrode surface. Two typical PTL-electrodes (bilayer vs single layer) were used to demonstrate how the electrode structure could impact device performance by affecting the bubble dynamics, electrolyte supply, and electrode utilization. 1D continuum model results show that the PTL-electrode is highly utilized close to the AEM, and less torturous structures with smaller pore radii in this region can enhance overall performance. An established and facile etching technique was used to modify the fiber surface of PTL-electrodes to improve activity and achieve an AEMWE performance of 2.3 A cm^{-2} at 1.8 V. Ultimately, this work demonstrates the prospects and identifies pathways for using PTL-electrodes to exceed the performance metrics necessary for AEMWEs to achieve commercial viability and accelerate the deployment of more affordable AEM water electrolysis technology for green hydrogen production.

4. Experimental Section

Materials and Chemicals: Stainless steel felt (10FP3, 15FP3, 10AL3), nickel felt (Ni 18–020), and platinized titanium felt (2GDL10-0.25) were purchased from Bekaert. PiperION A membranes (80 µm) and ionomer dispersions (5 wt% in ethanol) were purchased in bicarbonate form from Versogen, Inc. Platinum on carbon (46.3 wt% Pt) was purchased from TANAKA (TKK). Potassium hydroxide pellets (85%) were purchased from Fisher Chemical. Iridium oxide (IrO$_2$, Premion 99.99% metal basis) was purchased from Alpha Aesar. Cobalt oxide (Co$_3$O$_4$, >99.5%,

30–50 nm) was purchased from US Research Nanomaterials, Inc. Carbon paper (Toray 120, 10 wt% PTFE) and carbon black (Vulcan XC-72R) was purchased from Fuel Cell Store. Ethylene Tetrafluoroethylene gasketing material was purchased from CS Hyde. Nitric acid (ACS reagent, 70%), dimethyl sulfoxide-d$_6$ (99.5 atom% D), and n-Propanol (ACS reagent, ≥99.5%) were purchased from Sigma-Aldrich. Hydrochloric acid (36.5–38%) was purchased from VWR. Nafion dispersion (D2020, 20 wt%) was purchased from Ion Power. Deionized water (18 MΩ cm) was produced in-house using a Milli-Q (EMD Millipore).

Catalyst Coated Substrate Fabrication: A detailed description of electrode fabrication can be found in a previous report.[25] Briefly, cathode microporous layer (MPL) ink was prepared by bath sonicating carbon black with Nafion (I:C = 0.5) in a solvent of 1:9 v/v water:IPA. Cathode catalyst inks were prepared by bath sonicating a mixture of Pt/C and PiperION A (I:C = 0.5) in 1:9 v/v water:IPA for 40 min. Anode catalyst inks were prepared by tip sonicating a mixture of the catalyst (IrO$_x$ or Co$_3$O$_4$) in a 1:9 v/v water:IPA solvent for 10 min. After tip sonication, the ionomer was added (I:C = 0.2) and the ink was bath sonicated for 30 min. Ink solids content was ≈2 wt%.

The gas diffusion layer (GDL) for the cathodes and porous transport layer (PTL) for anodes were precisely cut to 30.25 cm^2. Inks for were airbrushed (Iwata Eclipse HP-CS) onto the substrate until the desired loading was reached: ≈1.0 mg$_C$ cm^{-2} for the cathode MPL, ≈0.5 mg$_{Pt}$ cm^{-2} for the cathode catalyst layer, and 1.0–2.0 mg$_{cat}$ cm^{-2} for the anode catalyst layer.

Membrane Electrode Assembly and Testing: The membrane (PiperION A, 80 µm) was stored in 1 M KOH and soaked for at least 24 h before use to ion exchange the carbonates with hydroxides. The cathode was cut using a 5 cm^2 punch die. The anodes were cut to 5 cm^2 using a Fiber 50 FC (Full Spectrum LASER) laser cutter. Before testing, the membrane, cathode, and anode are soaked in fresh 1 M KOH

**ADVANCED
SCIENCE NEWS**

www.advancedsciencenews.com

**ADVANCED
ENERGY
MATERIALS**

www.advenergymat.de

for 1 h. The membrane electrode assembly (MEA) was assembled with a standard Fuel Cell Technology cell, using a 25 cm² graphite serpentine flow field on the cathode and a 25 cm² nickel serpentine flow field on the anode. The flow fields were gasketed down to have an active area of 5 cm.² Combinations of 10, 2, and 1 mil EFTE gaskets were used to seal the cell and ensure 20–25% compression of the gas diffusion electrode (GDE). The thickness of the gaskets on the anode was adjusted to match the thickness of the porous transport electrode (PTE). The cell was compressed to 40 in-lbs in 10 in-lbs increments, following a star pattern.

Unless otherwise stated, cell testing was conducted at 80 °C with 1.0 M KOH as the anolyte and catholyte with a flow rate of 50 mL min⁻¹. Electrolyzer performance for 5 cm⁻² cells was measured using a Biologic VSP potentiostat with a 20 A booster (VMP3B-20) for current densities of 4 A cm⁻² or less and with a 200 A booster (FlexP 0012) for current densities above 4 A cm⁻². The 200 A booster was not set up with water cooling, and could only be safely operated up to 100 A. To break-in the cell, the current density was held at 1 A cm⁻² for 1 min, followed by two chronopotentiometric polarization curves with 10 s holds at each current density up to 4 A cm⁻² or a cell voltage of 3 V. After break-in, the double layer capacitance of the anode was measured using the Pt cathode as a reference. The double-layer capacitance was measured between 0.3 and 0.4 V with sweep rates of 50, 75, 100, 125, and 150 mV s⁻¹. For select cells after testing, the double layer capacitance of the anode was measured again.

Polarization curves were measured via chronopotentiometry, with each current density held for 1 min. The steady-state potential for each current density was taken as the average potential over the last 10 s of each hold. Galvanostatic electrochemical impedance spectroscopy (GEIS) was performed at each current density, up to 4 A cm⁻², after the 1 min hold. The signal was modulated by either 5% of the current density or 40 mA cm⁻² (lesser of the two), from a frequency of 1 MHz to 1 Hz with ten frequencies per decade. The high-frequency resistance (HFR) was determined by fitting the GEIS with an equivalent circuit consisting of a series combination of a resistor and two RCPEs. For 25 and 50 cm⁻² cells, only polarization curves were measured using the 200 A booster.

Accelerated Stress Testing (ASTs): Accelerated stress testing was performed with a dry cathode and with a 1.0 M KOH feed to the anode. The cell was subjected to current cycling between 2 and 0.5 A cm⁻² (5 s at each current) applied in a square wave fashion. Every 10000 cycles (≈28 h), polarization curve, EIS, and double layer capacitance were measured. DI water (≈100 mL) was added to the electrolyte daily to maintain a constant KOH concentration.

Durability (Constant Current Hold): The cell assembly and initial polarization curve measurement were performed as described above. The cell was operated with a dry cathode (capped off) and with a 0.1 M KOH feed to the anode. The anolyte reservoir was 2.2 L to minimize the impacts of water consumption. Current was supplied using an Agilent 6033A System Power Supply and the cell voltage was recorded every 15 min using an Agilent 34410A Multimeter. The electrolyte was replenished with ≈150 mL of DI water every 24 h to maintain a constant KOH concentration during the experiment. After the durability experiment, the cell was disassembled and the PTL-electrode was directly transferred and assembled into a fresh cell without any treatment.

Hydrogen Cross-Over Measurement: Hydrogen cross-over was determined by measuring the concentration of hydrogen in the anode oxygen effluent using an SRI Instruments 8610C gas chromatograph equipped with a thermal conductivity detector (TCD). The concentration was averaged over three injections.

X-Ray Photoelectron Spectroscopy (XPS): X-ray photoelectron spectra were collected using an XPS Kratos Axis Ultra DLD system with a monochromatic Al Kα source (hν = 1486.6 eV). Spectral analysis was performed using CasaXPS software and binding energies were calibrated to the C 1s signal at 284.8 eV.

Scanning Electron Microscopy (SEM): Scanning electron microscope images were taken using a FEI Quanta FEG 250 instrument under a high vacuum (10⁻⁵ Torr) with a beam energy of 10 kV. Cross-sectional PTL samples were prepared by casting the sample in a transparent epoxy. After curing, the samples were cross-sectioned, and the surface was polished and

sputtered with a thin layer of gold for improved conductivity. A detailed procedure is described in a previous report.[70]

X-Ray Fluorescence Spectroscopy (XRF): X-ray fluorescence spectra were collected using a Bruker M4 Tornado instrument. The platinum signal intensity was calibrated using standards ranging from 4 to 570 µg cm⁻².

Nuclear Magnetic Resonance (NMR): Membrane sample (≈20 mg) was dissolved in DMSO-d₆ (≈1.5 mL) and filtered using a 0.45 µm glass microfiber syringe filter. Nuclear magnetic resonance (NMR) spectra were collected using a Bruker Ascend 500 MHz instrument. Proton (¹H) NMR spectra were collected between $\delta_H = -3.8$ ppm and $\delta_H = 16.2$ ppm, with 64 scans per spectrum. Spectra were calibrated to the DMSO peak at $\delta_H = 2.5$ ppm. ¹H-¹³C heteronuclear single quantum coherence (HSQC) NMR spectra were collected using the standard "hsqcetgpsisp2.2" pulse program (acquisition time: 0.455 s, recycle delay: 3 s). The number of time increments recorded in the ¹³C direction was 1024. The number of points collected in the ¹H direction was 4096, with 16 scams per increment. Spectra were calibrated to the DMSO peak at $\delta_C/\delta_H = 39.5/2.5$ ppm.

Fourier-Transform Infrared (FTIR) Spectroscopy: Spectra were collected using a Bruker Vertex 70 FTIR spectrometer (Bruker, Billerica, MA) equipped with a liquid nitrogen-cooled mercury cadmium telluride (MCT) detector and a CO2-free dry air purge. A VariGATR ATR accessory (Harrick Scientific Products, Inc. NY) with a hemispherical Ge ATR crystal was used. The crystal was cleaned with 18.2 MΩ cm water and isopropyl alcohol between measurements. The incidence angle was set at 63°. The spectra signal was averaged over 200 scans at 4 cm⁻¹ resolution with an 8 mm aperture size and a nitrogen purge at ambient temperature. The used membrane was brittle and therefore water was added to the membrane to improve the surface contact with the ATR crystal.

X-Ray Computed Tomography (XCT): All XCT measurements for the PTL samples were conducted at Beamline 8.3.2 of the Advanced Light Source at Lawrence Berkeley National Laboratory in Berkeley, California, USA. The image acquisition was performed using white light mode for X-ray energy. For the images, a resolution of 0.65 µm pix⁻¹ was achieved using a 50 µm LuAG:Ce scintillator, sCMOS PCO edge camera, and an optical magnification of 10x. The tomography scans for each PTL sample were conducted at an exposure time of 80 ms per projection with 2625 projections in total while the sample was rotated from 0° to 180°. The tomography image datasets were reconstructed using TomoPy and Gridrec algorithms to produce image stacks with 2160 slices. The reconstruction parameters have been reported in previous works.[71–72] The image stacks were converted to 8 bits and image processing was completed using Fiji ImageJ. The images were thresholded and cropped manually, and the porosities and pores size distributions were calculated using ImageJ macros and plugins. Tortuosity was calculated using the TauFactor Python application.

Modeling: A 1D, two-phase, continuum AEMWE model was implemented using COMSOL Multiphysics software. The simulation domain consists of the anion-exchange-membrane (AEM), anode porous transport layer (aPTL), cathode catalyst layer (cCL), and cathode porous transport layer (cPTL), constructed based on the experimental. While the AEM and cCL domains were kept the same, aPTL domain was adjusted to investigate three different PTL configurations. The aPTL domain dimensions, materials, and the key parameters are listed in Table S3 (Supporting Information). Governing equations are solved under the following assumptions: steady state, laminar fluid flow, isotropic and homogeneous physical properties, and thermal equilibrium between different phases. Oxygen bubble coverage at the anode is estimated using an empirical correlation as a function of superficial current density:[73]

$$\theta = 0.023 \left(\frac{i_{cell}}{A\ m^{-2}} \right)^{0.3} \tag{1}$$

where i_{cell} is the superficial current density approximated as:

$$i_{cell} = a_0\ t_{aPTL} i_0^{OER} \exp\left(\frac{\alpha_{OER} F}{RT} \eta \right) \tag{2}$$

The OER kinetics (reaction current) is described by Tafel equation:

$$i_{rxn}^{OER} = a_{eff} \ i_0^{OER} \exp\left(\frac{\alpha_{OER}F}{RT}\eta\right) \tag{3}$$

where a_0 is the nominal electrochemical surface area (ECSA), t_{aPTL} is the PTL layer thickness, i_0^{OER} is the exchange current density, α_{OER} is the transfer coefficient, and η is the overpotential. The catalyst surface covered by the oxygen bubbles is assumed to not participate in OER. The effective ECSA is calculated as:

$$a_{eff} = a_0 \ (1 - \theta) \tag{4}$$

where a_{eff} is the utilized ECSA which is not covered by oxygen bubbles. Similarly, the conductive ionic path in the PTL electrode is disrupted by oxygen bubbles. The effective OH^- conductivity in the aPTL was approximated as:

$$\kappa_{OH^-}^{eff} = \kappa_{OH^-} \ (1 - \theta) \tag{5}$$

More detailed model descriptions including all governing equations and model parameters can be found in r previous works.[67–68]

The oxygen evolution reaction (OER) kinetic parameters, the charge transfer coefficient (α_{OER}) and the exchange current density (i_0^{OER}), and the nominal OH^- conductivity (κ_{OH^-}) in the aPTL domain were fitted using the polarization curve of the single layer PTL (SL_8) and kept constant for all aPTL configurations. Currently, the model cannot describe more complex bubble and two-phase flow phenomena (i.e., the BL_4-8 PTL configuration) which will affect the effective electrolyte conductivity. In order to account for these influences in the model, the conductivity was fitted for the BL_4-8 configuration so that the modeled polarization curve better described the experimental polarization curve, while the other parameters were still kept constant.

Acid Treatment: The pickling solution (300 mL DI water, 50 mL 70% nitric acid, and 10 mL 35% hydrochloric acid) was heated to 60 °C (±5 °C). The PTL sample (30.25 cm^2) was massed beforehand. The sample was placed in the solution for 10 min, with vigorous stirring. Afterward, the sample was rinsed thoroughly with DI water and dried at 100 °C for 1 h before being massed again.

Three Electrode Measurements: Three electrode testing was conducted using 1 cm^2 PTL-electrode samples as the working electrode, an Ag/AgCl electrode as the reference, and a Pt wire as the counter electrode in 1.0 м KOH at room temperature. The PTL-electrode samples were conditioned with 10 cyclic voltammetry sweeps from 0.5 to 1.0 V versus Ag/AgCl, and the performance was measured with linear sweep voltammetry from 0.5 to 1.0 V versus Ag/AgCl at a rate of 10 mV s^{-1}. Potentiostatic EIS was measured at open circuit voltage (OCV) to determine the electrolyte resistance and perform iR correction.

Supporting Information

Supporting Information is available from the Wiley Online Library or from the author.

Acknowledgements

Conflict of Interest

The authors declare no conflict of interest.

Author Contributions

A.W.T. and X.P. conceived and directed the project. A.W.T. and J.R.S. fabricated electrodes and performed the electrolyzer testing. T.Y.E. and A.Z.W. developed and implemented the 1D AEMWE model. J.K.L. collected SEM images. W.O. and G.W. collected and analyzed XPS data. A.W.T. and D.I.K. performed membrane characterization and analysis. J.L. and I.Z. collected, processed, and analyzed the XCT data. A.W.T., J.K.L., T.Y.E., A.Z.W., and X.P. wrote and revised the manuscript. All authors contributed to the discussion of the results. X.P. supervised the project.

Data Availability Statement

The data that support the findings of this study are available on request from the corresponding author. The data are not publicly available due to privacy or ethical restrictions.

Keywords

[1] P. R. Shukla, J. Skea, A. Reisinger, *Mitigation of Climate Change*, WMO, IPCC Secretariat, Geneva, Switzerland **2022**.

[2] A. d. Pee, D. Pinner, O. Roelofsen, K. Somers, *Decarbonization of Industrial Sectors: The Next Frontier*, McKinsey & Company, New York **2018**.

[3] Forum I. T., *I. T. F. Transport Outlook 2019*, OECD Publishing, Paris **2019**.

[4] IEA, *The Future of Hydrogen*, International Energy Agency, Paris **2019**.

[5] D. A. Cullen, K. C. Neyerlin, R. K. Ahluwalia, R. Mukundan, K. L. More, R. L. Borup, A. Z. Weber, D. J. Myers, A. Kusoglu, *Nat. Energy* **2021**, *6*, 462.

[6] *Assessment of Green Hydrogen for Industrial Heat*, Deloitte, Amsterdam, Netherlands **2023**.

[7] L. Yang, H. Liu, Z. Qiao, P. Sun, D. Li, R. Jiang, S. Liu, Z. Niu, Y. Zhang, T. Lin, Q. Zhang, L. Gu, S. Wang, D. Cao, Z. Chen, *Adv. Energy. Mater.* **2023**, *13*, 2204390.

[8] H. Wu, C. Feng, L. Zhang, J. Zhang, D. P. Wilkinson, *Electrochem. Energy Rev.* **2021**, *4*, 473.

[9] N. Rambhujun, M. S. Salman, T. Wang, C. Pratthana, P. Sapkota, M. Costalin, Q. Lai, K.-F. Aguey-Zinsou, *MRS Energy Sustain* **2020**, *7*, E33.

[10] W. Schutyser, T. Renders, S. Van Den Bosch, S.-F. Koelewijn, G. T. Beckham, B. F. Sels, *Chem. Soc. Rev.* **2018**, *47*, 852.

[11] A. W. Tricker, S. Najmi, E. V. Phillips, K. L. Hebisch, J. X. Kang, C. Sievers, *RSC Sustainability* **2023**, *1*, 346.

[12] B. Lee, L. R. Winter, H. Lee, D. Lim, H. Lim, M. Elimelech, *ACS Energy Lett.* **2022**, *7*, 3032.

[13] A. W. Tricker, K. L. Hebisch, M. Buchmann, Y.-H. Liu, M. Rose, E. Stavitski, A. J. Medford, M. C. Hatzell, C. Sievers, *ACS Energy Lett.* **2020**, *5*, 3362.

[14] M. Chatenet, B. G. Pollet, D. R. Dekel, F. Dionigi, J. Deseure, P. Millet, R. D. Braatz, M. Z. Bazant, M. Eikerling, I. Staffell, P. Balcombe, Y. Shao-Horn, H. Schäfer, *Chem. Soc. Rev.* **2022**, *51*, 4583.

ADVANCED
SCIENCE NEWS

www.advancedsciencenews.com

ADVANCED
ENERGY
MATERIALS

www.advenergymat.de

[15] IEA, *Global Hydrogen Review*, International Energy Agency, Paris, **2021**.

[16] IEA, *Global Hydrogen Review*, International Energy Agency, Paris, **2022**.

[17] A. Godula-Jopek, *Hydrogen Production: By Electrolysis*, John Wiley & Sons, Hoboken, New Jersey **2015**.

[18] K. Zeng, D. Zhang, *Prog. Energy Combust. Sci.* **2010**, *36*, 307.

[19] J. D. Holladay, J. Hu, D. L. King, Y. Wang, *Catal. Today* **2009**, *139*, 244.

[20] M. Carmo, D. L. Fritz, J. Mergel, D. Stolten, *Int. J. Hydrog. Energy* **2013**, *38*, 4901.

[21] IRENA, *Green Hydrogen Cost Reduction*, International Renewable Energy Agency, Abu Dhabi **2020**.

[22] Z. Taie, X. Peng, D. Kulkarni, I. V. Zenyuk, A. Z. Weber, C. Hagen, N. Danilovic, *ACS Appl. Mater. Interfaces* **2020**, *12*, 52701.

[23] Q. Li, A. Molina Villarino, C. R. Peltier, A. J. Macbeth, Y. Yang, M.-J. Kim, Z. Shi, M. R. Krumov, C. Lei, G. G. Rodríguez-Calero, J. Soto, S.-H. Yu, P. F. Mutolo, L. Xiao, L. Zhuang, D. A. Muller, G. W. Coates, P. Zelenay, H. D. Abruña, *J. Phys. Chem. C* **2023**, *127*, 7901.

[24] L. Wan, Z. Xu, Q. Xu, M. Pang, D. Lin, J. Liu, B. Wang, *Energy Environ. Sci.* **2023**, *16*, 1384.

[25] A. W. Tricker, J. K. Lee, J. R. Shin, N. Danilovic, A. Z. Weber, X. Peng, *J. Power Sources* **2023**, *567*, 232967.

[26] N. Chen, Y. M. Lee, *Prog. Polym. Sci.* **2021**, *113*, 101345.

[27] M. Moreno-González, P. Mardle, S. Zhu, B. Gholamkhass, S. Jones, N. Chen, B. Britton, S. Holdcroft, *J. Power Sources Adv.* **2023**, *19*, 100109.

[28] N. Du, C. Roy, R. Peach, M. Turnbull, S. Thiele, C. Bock, *Chem. Rev.* **2022**, *122*, 11830.

[29] H. Yu, N. Danilovic, Y. Wang, W. Willis, A. Poozhikunnath, L. Bonville, C. Capuano, K. Ayers, R. Maric, *Appl. Catal., B* **2018**, *239*, 133.

[30] A. R. Motz, D. Li, A. Keane, L. D. Manriquez, E. J. Park, S. Maurya, H. Chung, C. Fujimoto, J. Jeon, M. K. Pagels, C. Bae, K. E. Ayers, Y. S. Kim, *J. Mater. Chem. A* **2021**, *9*, 22670.

[31] K. M. Hugar, H. A. Kostalik, G. W. Coates, *J. Am. Chem. Soc.* **2015**, *137*, 8730.

[32] J. Fan, A. G. Wright, B. Britton, T. Weissbach, T. J. G. Skalski, J. Ward, T. J. Peckham, S. Holdcroft, *ACS Macro Lett.* **2017**, *6*, 1089.

[33] J. Wang, Y. Zhao, B. P. Setzler, S. Rojas-Carbonell, C. Ben Yehuda, A. Amel, M. Page, L. Wang, K. Hu, L. Shi, S. Gottesfeld, B. Xu, Y. Yan, *Nat. Energy* **2019**, *4*, 392.

[34] J. S. Olsson, T. H. Pham, P. Jannasch, *Adv. Funct. Mater.* **2018**, *28*, 1702758.

[35] Z. Zhang, L. Wu, J. Varcoe, C. Li, A. L. Ong, S. Poynton, T. Xu, *J. Mater. Chem. A* **2013**, *1*, 2595.

[36] A. D. Mohanty, C. Bae, *J. Mater. Chem. A* **2014**, *2*, 17314.

[37] H. Sun, Z. Yan, F. Liu, W. Xu, F. Cheng, J. Chen, *Adv. Mater.* **2020**, *32*, 1806326.

[38] H. Schäfer, M. Chatenet, *ACS Energy Lett.* **2018**, *3*, 574.

[39] M. Kim, J. Ha, Y.-T. Kim, J. Choi, *Chem. Eng. J.* **2022**, *440*, 135459.

[40] B. Chen, A. L. G. Biancolli, C. L. Radford, S. Holdcroft, *ACS Energy Lett.* **2023**, *8*, 2661.

[41] R. A. Krivina, G. A. Lindquist, S. R. Beaudoin, T. N. Stovall, W. L. Thompson, L. P. Twight, D. Marsh, J. Grzyb, K. Fabrizio, J. E. Hutchison, S. W. Boettcher, *Adv. Mater.* **2022**, *34*, 2203033.

[42] J. K. Lee, G. Anderson, A. W. Tricker, F. Babbe, A. Madan, D. A. Cullen, J. D. Arregui-Mena, N. Danilovic, R. Mukundan, A. Z. Weber, X. Peng, *Nat. Commun.* **2023**, *14*, 4592.

[43] S. M. Alia, K. S. Reeves, H. Yu, J. Park, N. Kariuki, A. J. Kropf, D. J. Myers, D. A. Cullen, *J. Electrochem. Soc.* **2022**, *169*, 054517.

[44] S. Narayanaru, S. Miyanishi, H. Kuroki, G. M. Anilkumar, T. Yamaguchi, *ACS Sustainable Chem. Eng.* **2023**, *11*, 9281.

[45] F. Song, M. M. Busch, B. Lassalle-Kaiser, C.-S. Hsu, E. Petkucheva, M. Bensimon, H. M. Chen, C. Corminboeuf, X. Hu, *ACS Cent. Sci.* **2019**, *5*, 558.

[46] R. B. Kutz, Q. Chen, H. Yang, S. D. Sajjad, Z. Liu, I. R. Masel, *Energy Technol.* **2017**, *5*, 929.

[47] A. M. Barnes, B. Liu, S. K. Buratto, *Langmuir* **2019**, *35*, 14188.

[48] J. Park, Z. Kang, G. Bender, M. Ulsh, S. A. Mauger, *J. Power Sources* **2020**, *479*, 228819.

[49] A. T. Mayyas, M. F. Ruth, B. S. Pivovar, G. Bender, K. B. Wipke, *Manufacturing Cost Analysis for Proton Exchange Membrane Water Electrolyzers*, National Renewable Energy Lab.(NREL), Golden, CO, US **2019**.

[50] Ö. F. Selamet, F. Becerikli, M. D. Mat, Y. Kaplan, *Int. J. Hydrog. Energy* **2011**, *36*, 11480.

[51] Ö. F. Selamet, M. C. Acar, M. D. Mat, Y. Kaplan, *Int. J. Eng. Res.* **2013**, *37*, 457.

[52] S. Sun, Z. Shao, H. Yu, G. Li, B. Yi, *J. Power Sources* **2014**, *267*, 515.

[53] S. Ding, B. Guo, S. Hu, Z. Tian, J. Gu, T. Zhang, F. Yang, M. Ouyang, *Fuel* **2023**, *350*, 128799.

[54] P. Trinke, P. Haug, J. Brauns, B. Bensmann, R. Hanke-Rauschenbach, T. Turek, *J. Electrochem. Soc.* **2018**, *165*, F502 .

[55] A. P. Grosvenor, M. C. Biesinger, R. S. C. Smart, N. S. Mcintyre, *Surf. Sci.* **2006**, *600*, 1771.

[56] M. N. K. Safeer, C. Alex, R. Jana, A. Datta, N. S. John, *J. Mater. Chem. A* **2022**, *10*, 4209.

[57] T. Yamashita, P. Hayes, *Appl. Surf. Sci.* **2008**, *254*, 2441.

[58] J. Xiao, A. M. Oliveira, L. Wang, Y. Zhao, T. Wang, J. Wang, B. P. Setzler, Y. Yan, *ACS Catal.* **2020**, *11*, 264.

[59] H. Sun, Z. Yan, F. Liu, W. Xu, F. Cheng, J. Chen, *Angew. Chem.* **2021**, *133*, 19421.

[60] R. A. Krivina, G. A. Lindquist, M. C. Yang, A. K. Cook, C. H. Hendon, A. R. Motz, C. Capuano, K. E. Ayers, J. E. Hutchison, S. W. Boettcher, *ACS Appl. Mater. Interfaces* **2022**, *14*, 18261.

[61] G. A. Lindquist, Q. Xu, S. Z. Oener, S. W. Boettcher, *Joule* **2020**, *4*, 2549.

[62] M. Zlobinski, T. Schuler, F. N. Büchi, T. J. Schmidt, P. Boillat, *J. Electrochem. Soc.* **2021**, *168*, 014505.

[63] J. K. Lee, C. Lee, K. F. Fahy, P. J. Kim, J. M. Lamanna, E. Baltic, D. L. Jacobson, D. S. Hussey, S. Stiber, A. S. Gago, K. A. Friedrich, A. Bazylak, *Energy Convers. Manage.* **2020**, *226*, 113545.

[64] Q. Xu, S. Z. Oener, G. Lindquist, H. Jiang, C. Li, S. W. Boettcher, *ACS Energy Lett.* **2020**, *6*, 305.

[65] N. U. Hassan, E. Motyka, J. Kweder, P. Ganesan, B. Brechin, B. Zulevi, H. R. Colón-Mercado, P. A. Kohl, W. E. Mustain, *J. Power Sources* **2023**, *555*, 232371.

[66] Y. Chen, F. Mojica, G. Li, P.-Y. A. Chuang, *Int. J. Eng. Res.* **2017**, *41*, 2365.

[67] J. Liu, Z. Kang, D. Li, M. Pak, S. M. Alia, C. Fujimoto, G. Bender, Y. S. Kim, A. Z. Weber, *J. Electrochem. Soc.* **2021**, *168*, 054522.

[68] J. Liu, A. Z. Weber, *J. Electrochem. Soc.* **2022**, *169*, 054506.

[69] L.-F. Li, J.-P. Celis, *Can. Metall. Q.* **2003**, *42*, 365.

[70] J. K. Lee, G. Y. Lau, M. Sabharwal, A. Z. Weber, X. Peng, M. C. Tucker, *J. Power Sources* **2023**, *559*, 232606.

[71] A. D. Shum, D. Y. Parkinson, X. Xiao, A. Z. Weber, O. S. Burheim, I. V. Zenyuk, *Electrochim. Acta* **2017**, *256*, 279.

[72] A. Serov, A. D. Shum, X. Xiao, V. De Andrade, K. Artyushkova, I. V. Zenyuk, P. Atanassov, *Appl. Catal., B* **2018**, *237*, 1139.

[73] H. Vogt, R. J. Balzer, *Electrochim. Acta* **2005**, *50*, 2073.